Prediction and Analysis of EMI Spectrum Based on the Operating Principle of EMC Spectrum Analyzers

Le Yang, *Student Member, IEEE*, Shuo Wang, *Fellow, IEEE*, Hui Zhao, *Student Member, IEEE*, and Yongjian Zhi

***Abstract*—EMC spectrum analyzers are popularly used for electromagnetic interference (EMI) measurement in power electronics systems. Depending on the specifications of EMI standards, the EMI measurement could be very time consuming. Conventionally, the fast Fourier transform is used to derive the EMI spectrum from the measured time-domain waveforms. However, these results may not agree with the measurement results from spectrum analyzers, and sometimes the difference could be significant. In this paper, a technique to quickly and accurately predict and analyze the EMI spectrum from time-domain waveforms is proposed. The technique is developed based on the spectrum analyzer's operating principle and the requirements of EMI standards. The EMI spectra of three modulation schemes are also analyzed. Theoretical analysis, simulations, and experiments were all conducted. The predicted peak, quasi-peak, and average EMI matches the measured EMI in whole conductive frequency range. The developed technique can accurately predict EMI using much shorter time than conventional EMC spectrum analyzers and it saves cost of expensive spectrum analyzers.**

***Index Terms*—Electromagnetic interference (EMI) noise prediction, envelope detector, resolution bandwidth (RBW), sideband effect, spectrum analyzer.**

I. Introduction

ELECTROMAGNETIC interference (EMI) degrades power electronics system's reliability and shortens power components' lifespan [1], [2]. Commercial switching power converters or inverters must comply with the EMI standards such as CISPR standards [3] before they can be sold on the market. Accurate EMI prediction can help debug and suppress EMI [4], so it has drawn a lot of attentions in recent years.

Fast Fourier transform (FFT) was applied to the time-domain voltage waveforms on the line impedance stabilization network (LISN) to extract the EMI spectrum [1], [5], [6] for EMI prediction, analysis, and reduction. However, because EMI standards have specific requirements on the resolution bandwidth (RBW), the envelope detector, the peak detector, the quasi-peak detector, and the average detector for spectrum analyzers, the FFT results, which do not consider the influence of these requirements, may not agree with actual measurement results.

Manuscript received November 13, 2018; revised March 9, 2019; accepted April 17, 2019. Date of publication May 1, 2019; date of current version October 18, 2019. This work was supported by the CRRC Zhuzhou Institute Co., Ltd. Recommended for publication by Associate Editor A. Lindemann. *(Corresponding author: S. Wang.)*

L. Yang and S. Wang are with the University of Florida, Gainesville, FL 32611 USA (e-mail: yanglemike@ufl.edu; shuowang@ieee.org).

H. Zhao is with the University of Cambridge, Cambridge CB2 8PQ, U.K. (e-mail: hz352@cam.ac.uk).

Y. Zhi is with the CRRC Zhuzhou Institute Co., Ltd., Zhuzhou 412001, China (e-mail: zhiyj@csrzic.com).

Color versions of one or more of the figures in this paper are available online at http://ieeexplore.ieee.org.

Digital Object Identifier 10.1109/TPEL.2019.2914468

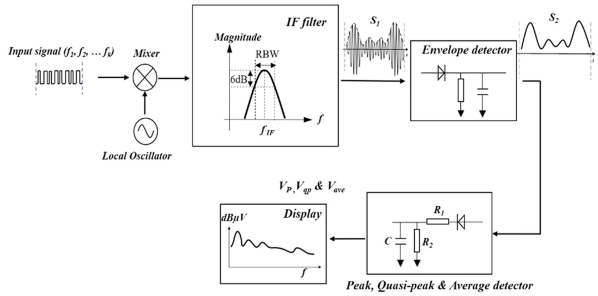

Fig. 1. Operating principle of the peak, quasi-peak and average noise measurement in a spectrum analyzer (150 kHz–30 MHz)

EMC spectrum analyzers measure the EMI spectrum differently from FFT. The FFT can find the magnitude and phase of EMI harmonics based on time-domain waveforms. However, the EMC spectrum analyzers process harmonics differently from FFT. As a result, FFT may not have the same result as an EMC spectrum analyzer.

A typical quasi-peak EMI measurement in a spectrum analyzer is illustrated in Fig. 1 [9], [12] based on CISPR 16.

Fig. 1, the input noise has a spectrum including harmonic frequencies $f_1, f_2, \ldots f_k \ldots$. The spectrum is mixed with a signal generated by a local oscillator. The signal generated by the local oscillator has a frequency $f_{\rm LO}$. The $f_{\rm LO}$ is tunable and is equal to $f_{\rm LS} + f_{\rm IF}$. $f_{\rm IF}$ is the intermediate frequency (IF) of an IF filter connected to the output of the mixer. The output of the mixer has a spectrum including frequencies $f_{\rm LO} + f_1$, $f_{\rm LO} - f_1$, $f_{\rm LO} + f_2$, $f_{\rm LO} - f_2, \ldots, f_{\rm LO} + f_k$, $f_{\rm LO} - f_k, \ldots$ and other frequency components. The amplitude of the signal with frequency $f_{\rm LO} - f_k = f_{\rm LS} + f_{\rm IF} - f_k$ is proportional to the product of the amplitudes of signals $f_{\rm LO}$ and f_k. The output of the mixer is fed to the IF filter. The IF filter has 9 kHz 6 dB RBW as shown in Fig. 1. The IF filter has zero attenuation to the signal at $f_{\rm IF}$. For the signal not at $f_{\rm IF}$, the attenuation can be approximately characterized with a Gaussian function [12]. The local oscillator can sweep $f_{\rm LO}$ within the whole concerned frequency range, for example from 150 kHz to 30 MHz. For those f_k, which is close to $f_{\rm LS}$ so that $f_{\rm LO} - f_k$ is located within the effective bandwidth of an IF filter, can pass through the IF filter due to its small attenuations. The waveform S_1 in Fig. 1 is an example of the output of the IF filter.

The IF signal is fed to an envelope detector. The envelope detector can follow the fastest possible changes of the

envelope of the IF signal (IF filter's bandwidth determines the fastest changes) but not the instantaneous value of the IF waveform itself. The waveform S_2 in Fig. 1 is an example of the output of an envelope detector. The envelope signal is further fed to a quasi-peak detector in Fig. 1. The quasi-peak detector has a charging time constant τ_C and discharging time constant τ_D defined in EMI standards.

In Fig. 1, the capacitor C in the quasi-peak detector was charged up when the output of the envelope detector is higher than the voltage on C. On the other hand, it is discharged all the time through R_2. The voltage on C reaches steady state when its charge is balanced.

For average or peak noise measurement, the quasi-peak detector in Fig. 1 is replaced with an average or a peak detector. The other components in Fig. 1 are exactly the same. The difference between quasi-peak detector and the other two detectors is the charging and discharging time constants. For example, the average detector is basically a low-pass filter, which retains the dc component in the output of the envelope detector. On the other hand, the peak detector has a very small charging time constant.

In [8], the EMC spectrum analyzer is implemented with the simulation circuits based on Fig. 1. However, the simulation could be very time consuming due to the required good simulation resolution and response time of the IF filter and the detectors in Fig. 1. Li and See [10], and Karaca *et al.* [11] proposed a method to drive quasi-peak and average values by adding conversion factors, which are functions of RBW and pulse repetition frequency, to the peak EMI value of sequential impulses with a fixed duty cycle. However, in power electronics applications, the noise current has different duty cycles from that used in these papers. Furthermore, the duty cycle may be time varying too. For example, the sinusoidal pulsewidth modulation (SPWM) waveforms and switching frequency jittering waveforms are much different from the sequential impulse signal used in the papers. As a result, the conversion factors cannot be used to predict EMI. Wang *et al*. [12] and Ruan and Ye [13] predict the quasi-peak EMI of a power factor correction (PFC) converter. However, the effects of sidebands on the measured EMI were not analyzed. Moreover, in the paper, only the frequency component with the highest magnitude is used as an envelope. This envelope detector model is not accurate enough when there are more than one large-magnitude frequency components at the output of the IF filter. Nussbaumer *et al.* [15], [16] investigated the influence of sidebands of the switching frequency components to the measured EMI. However, none of these papers give the accurate prediction algorithm for quasi-peak and average values. Only the "worst case" and the range of quasi-peak are derived.

In this paper, an EMI prediction technique is developed based on an improved IF filter model, an improved envelope detector model and the functional blocks of the spectrum analyzer in Fig. 1. Section II develops a modeling technique for spectrum analyzer based on the function blocks in Fig. 1 and proposes a procedure for EMI prediction based on time-domain waveforms. Section III analyzes the effects of sideband and effective RBW on EMI measurement. The EMI of constant pulsewidth modulation (CPWM), SPWM, and switching frequency modulation (SFM) is analyzed and compared. The difference between FFT and the spectrum analyzer's measurement results is analyzed based on the effects of effective RBW and sideband on EMI. The condition of minimizing EMI with SFM is also discussed. Section IV conducts experiments to validate the developed EMI prediction and analysis technique for the three different modulation techniques in Section III.

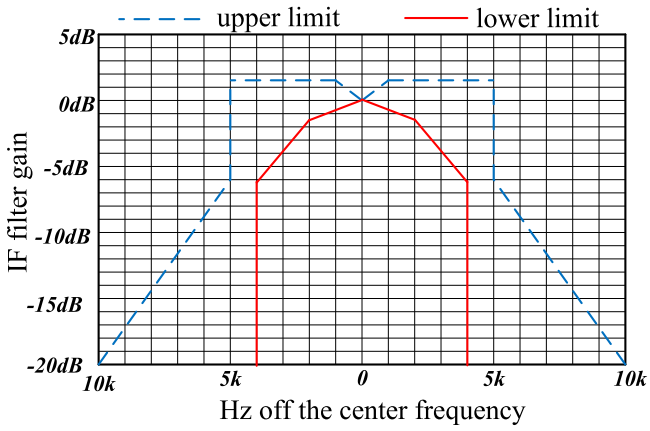

Fig. 2. 9 kHz IF gain region defined by CISPR 16.

II. Spectrum Analyzer Modeling and EMI Prediction

In this section, based on the operating principle of EMC spectrum analyzers, the modeling technique is developed to accurately characterize the spectrum analyzer and predict EMI. Compared with existing references [8], [10]–[13], [15], and [16], the contribution of this paper on the spectrum analyzer modeling is—first, developed more accurate IF filter Gaussian function based on actual spectrum analyzers; and second, derived a general envelope detector model, which includes the magnitude of the vector sum of all frequency components within effective RBW, so it is more accurate than existing techniques.

A. Accurate IF Filter Modeling

The IF filter's transfer function can be expressed by a Gaussian function [12]

$$G_{\mathrm{IF}}(f,c)=\exp\left(-(f-f_{\mathrm{IF}})^2/c^2\right) \tag{1}$$

where f is the noise signal frequency, f_{IF} is the intermediate frequency of the IF filter and c is given by [12]

$$c=\frac{\mathrm{RBW}}{2\sqrt{\ln 2}}. \tag{2}$$

Since the magnitude and -6 dB bandwidth of the IF filter's transfer function is defined by a region in EMI standards, such as CISPR 16 in Fig. 2, different EMI standards or different spectrum analyzers may have different IF filter gains.

The gains of IF filters in spectrum analyzers may not follow (1) and (2) exactly. As a result, different IF filter gains may have several dB or more difference in the final EMI measurement results. Because of this, a fixed Gaussian function expression cannot always agree with the IF filter gains in different EMI measurement equipment.

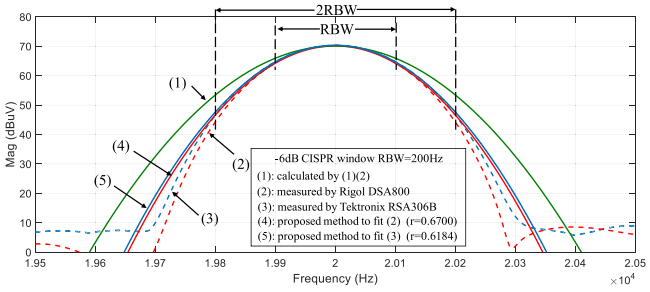

Fig. 3. Comparison of the measured and calculated IF filter gains for 200 Hz RBW.

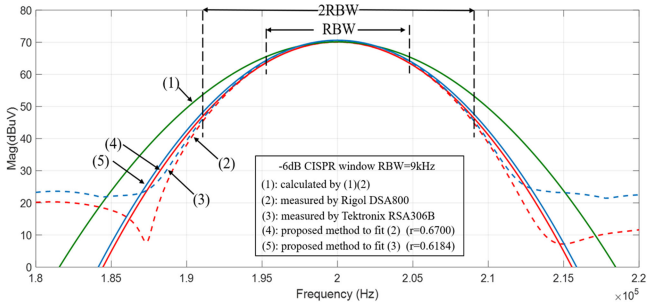

Fig. 4. Comparison of the measured and calculated IF filter gains for 9 kHz RBW.

In Fig. 1, the IF filter gain of a spectrum analyzer can be simply estimated by observing the measured peak spectrum of a signal with fixed magnitude and frequency. This is because when the spectrum analyzer sweeps f_{LO}, the gain of the IF filter shapes the spectrum of the signal at the output of the IF filter [9]. In Figs. 3 and 4, the -6 dB RBW is 200 Hz from 9 to 150 kHz and 9 kHz from 150 kHz to 30 MHz in CISPR16. The IF filter gains of the spectrum analyzer Rigol DSA800 and Tektronix RSA 306B from 10 to 150 kHz and from 150 kHz to 30 MHz were measured with the method above by feeding 20 and 200 kHz sinusoidal signal, respectively. The calculated IF filter gain based on (1) and (2) are also compared in the figures. It is shown that there is several-dB difference at one-RBW boundary and around 10 dB difference at two-RBW boundary between the measured and the calculated IF filter gains. It will be shown later that the frequency components outside of RBW may still contribute to the final EMI results, so filter gain must be accurately modeled. The parameter c in (1) determines the shape of the IF filter gain, so it must be accurately determined based on the measured IF filter gains of actual spectrum analyzers. Equation (2) should therefore be improved.

In this paper, a technique is proposed below to accurately determine Gaussian function. Equation (2) was modified to (3)

$$c = \mathrm{RBW} \times r. \tag{3}$$

In (3), r is a coefficient which has the bandwidth and attenuation information of the Gaussian function. Based on (1), (3) and the IF filter gains of Rigol DSA800 and RSA306B in Figs. 2 and 3, r can be determined using curve fitting function in MATLAB and it was found $r = 0.67$ and 0.6184, respectively, for CISPR window. With this new c, the Gaussian functions match the measured gains well in Figs. 3 and 4. The same technique can be applied to determine r for the other IF filter windows, such as Kaiser window. For the data outside of 2 RBW, its value is much smaller than those close to center frequency. These small data will have very small weight factors in MATLAB's fitting process, which means they are less important than those data near the center frequency. Because of this, the result from MATLAB shows some difference from the measured result outside of 2 RBW. However, the difference will not introduce significant error at the output of the IF filter because the signals outside two RBW range are largely attenuated. Also, even the signals outside two RBW are much larger than the center frequency component, they will not bring significant influence on the EMI spectrum measurement. This issue will be discussed in Section III.

The technique proposed here can be considered as a calibration of the Gaussian function of an IF filters for different EMI standards and spectrum analyzers when the EMI is to be predicted without using spectrum analyzers to save time and cost on EMI measurement. Also, because the IF filters used in spectrum analyzers are finite impulse response filters, which have identical time delay [27] to all frequency components, the IF filters do not introduce phase shift to the frequency components.

B. Accurate Envelope Detector Modeling

In [12] and [13], the output of the envelope detector at a frequency was modeled with the frequency component with the maximum magnitude within a set of frequency components at the output of the IF filter. However, these frequency components have phases, so in time domain, the magnitude, which determines the envelope, of the vector sum of all of these frequency components is not equal to the maximum magnitude of these frequency components. To accurately model the envelope detector, the magnitude of the vector sum of these frequency components must be considered. In general, *s(t)* in (4) represents the signal including different frequency components fed to the envelope detector from the IF filter. In (4), A_i, ω_i, and θ_i are the magnitude, frequency, and phase of the ith frequency component, respectively. p is the number of frequency components

$$s(t) = A_1 \cos(\omega_1 t + \theta_1) + A_2 \cos(\omega_2 t + \theta_2) + \cdots + A_p \cos(\omega_p t + \theta_p). \tag{4}$$

Taking frequency ω_1 and phase θ_1 as the frequency and phase references, (4) becomes

$$s(t) = A_1 \cos(\omega_1 t + \alpha_1) + A_2 \cos(\omega_1 t + \alpha_2) + \cdots + A_p \cos(\omega_1 t + \alpha_p) \tag{5}$$

where $\alpha_i = (\omega_i - \omega_1)t + \theta_i$. Equation (5) can be further simplified to (6).

$$s(t) = c(t) \cos(\omega_1 t + \varphi) \tag{6}$$

c(t) in (6) represents the envelope and it is given by

$$c(t) = \sqrt{\left(\sum_{i=1}^{p} A_i \cos(\alpha_i)\right)^2 + \left(\sum_{i=1}^{p} A_i \sin(\alpha_i)\right)^2}. \tag{7}$$

TABLE I
FREQUENCY COMPONENTS FED TO AN ENVELOPE DETECTOR

	f(Hz)	*Mag (mV)*	*Phase (degree)*
$S_1(t)$	29760	7.58	168
$S_2(t)$	29820	4.78	-30.5
$S_3(t)$	29880	14.30	148.1
$S_4(t)$	30000	13.23	-41.5
$S_5(t)$	30120	14.18	133.4
$S_6(t)$	30180	4.05	185.9
$S_7(t)$	30240	7.94	139.5

In (7), the ac and dc components of the envelope can be represented in (8).

$$c(t) = \sqrt{\underbrace{\sum_{i=1}^{p} A_i^2}_{\text{dc}} + \underbrace{\left(\sum_{k=1}^{p}\sum_{j=1}^{p} A_k A_j \cos\left(\omega_k t - \omega_j t + \theta_k - \theta_j\right)\right)}_{\text{ac components}}} \tag{8}$$

In the equations above, for switching mode power electronics applications, if f_s is the switching frequency of a constant-frequency and constant-duty cycle (CPWM) waveform, the period T_s of the envelope of the CPWM waveform is $1/f_s$. For any harmonic components ω_k and ω_j, condition $(\omega_k - \omega_j)/2\pi = nf_s$ is always met, where $n = |k - j|$ and $j \neq k$. For a SPWM waveform, $(\omega_k - \omega_j)/2\pi = nf_{\text{md}}$, where $n = |k - j|, j \neq k$, and f_{md} is modulation frequency [14]. Equation (8) indicates that the period T_S of the envelope is $1/f_s$ or $1/f_{\text{md}}$. *c(t)* is equal to the square root of the sum of a dc component, which is equal to the sum of A_i^2 and ac components that include all of the cross-product terms in (7). The magnitude of the ac components in (8) is a function of both the magnitudes and phases of the frequency components in (4).

As an example, Table I shows the magnitudes and phases of seven frequency components around 30 kHz of a SPWM waveform modulated at $f_{\text{md}} = 60$ Hz. The envelope of these seven frequency components is calculated based on (8) as the red curve shows in Fig. 5. The simulated time-domain waveform of these seven frequency components is shown as blue curves in Fig. 5. The calculated matches the simulated envelopes very well. Also, as expected in (8), the period $1/f_{\text{md}}$ of the envelope is 1/60 Hz = 0.0167 s, which is equal to the least common multiple of these seven frequency components.

Compared with the spectrum analyzer circuit simulation model in [8], the proposed technique is faster as it does not need wait long time for the simulation circuit to reach steady state. Also, the small simulation step to guarantee the accuracy in the simulations reduces the simulation speed [8]. On the other hand, because the envelope at the output of the IF filter is directly calculated from (8), there is no simulation step issue for the proposed technique.

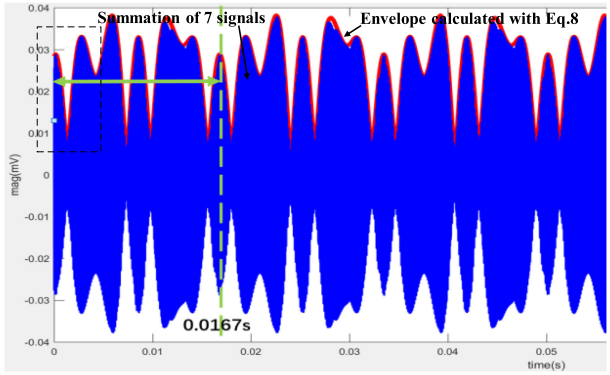

Fig. 5. Verification of the developed envelope detector model.

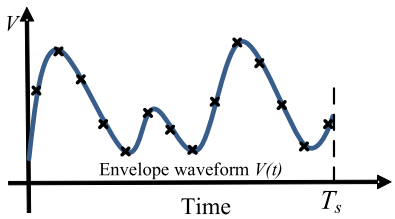

Fig. 6. Digital sampling on the envelope waveform to determine the peak and average value.

TABLE II
CHARGING AND DISCHARGING TIME CONSTANTS OF QUASI-PEAK DETECTORS

	Band A: 9 kHz-150 kHz	Band B: 150 kHz-30 MHz	Band C/D: 30 MHz-1 GHz
RBW	200 Hz	9 kHz	120 kHz
T_D	500 ms	160 ms	550 ms
T_C	45 ms	1 ms	1 ms

C. Peak, Quasi-Peak, and Average Detection

Based on the envelope waveform, the peak, quasi-peak, and average values can be determined by the detector circuit with different charging and discharging time constants in Fig. 1. One period of waveform in Section II-B should be investigated for peak, quasi-peak, and average detection as it includes all the information.

In the process of obtaining the peak and average values of the envelope in one period, the digital sampling is applied. If there are *N* evenly sampled data in one period as shown in Fig. 6, the peak value V_{peak} of the envelope is the maximum value of these sampled data V_i in (9).

For quasi-peak detection, CISPR standards define the charging and discharging time constants in Table II for the quasi-peak detector circuit in Fig. 7(a). R_c, R_d, C, V_{envelope}, and $V_{\text{quasi-peak}}$ are charging resistance, discharging resistance, charging capacitor, input envelope voltage, and output quasi-peak voltage of the quasi-peak detector, respectively.

$$V_{\text{peak}} = \max(V_i). \tag{9}$$

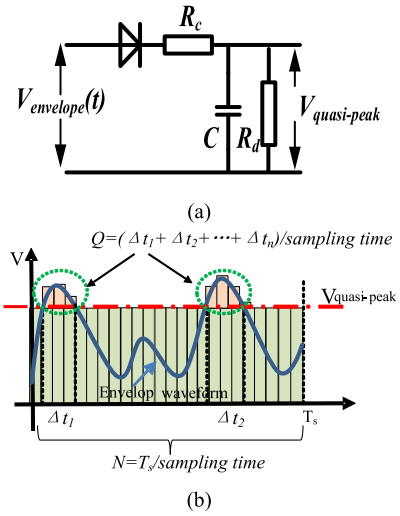

Fig. 7. (a) Quasi-peak detector circuit. (b) Quasi-peak value based on capacitor charge balance.

The average value is given by (10) [22].

$$V_{\text{ave}} = \frac{\sum_{i=1}^{N} V_i}{N}. \tag{10}$$

Ignoring small ripples, the steady-state quasi-peak value $V_{\text{quasi-peak}}$ can be derived based on charge balance on the capacitor C [12]. The equation used to calculate the quasi-peak value based on sampled data in Fig. 7(b) is derived here in (11). Δt_i is the ith time interval when the envelope waveform V_{envelope} is larger than $V_{\text{quasi-peak}}$. Q is the number of the sampled data that are larger than $V_{\text{quasi-peak}}$.

$$\frac{\sum_{i=1}^{Q} (V_i - V_{\text{quasi-peak}})}{R_c} = \frac{V_{\text{quasi-peak}} \times N}{R_d}. \tag{11}$$

Based on (9), (10), and (11), $V_{\text{peak}} \geq V_{\text{quasi-peak}} \geq V_{\text{ave}}$. The equality holds when the output voltage V_i of the envelope detector has a dc component only.

D. Procedure of EMI Prediction

The EMI can be predicted based on the flow chart in Fig. 8. The time-domain voltage waveform is first sampled using an oscilloscope. Based on sampling theory, the sampling rate is at least twice of the highest concerned frequency. For conductive EMI from 9 kHz to 30 MHz, the sample rate should be more than 60 MSa/s. The sampled waveform is imported to MATLAB for FFT to extract frequency, phase, and magnitude information for all frequency components. In order not to lose the information of each frequency component, a good frequency resolution should be selected in FFT. Theoretically, the frequency resolution should be smaller than f_s or f_{md}. In this paper, a 10 Hz frequency resolution is selected in FFT that requires at least 0.1 s period of input signal.

The results of FFT are a series of sinusoidal signals with different frequencies, phases, and magnitudes. These signals are fed to the IF filter. The initial value of f_{IF} is equal to the starting frequency f_{start} of the concerned frequency range from f_{start} to f_{end}. Based on the proposed Gaussian function calibration technique in Section II-A, the IF filter gain should have been accurately characterized. To accurately predict EMI, all frequency components passing through the IF filter should be included for envelope detection. However, due to the limited bandwidth of the IF filter in Figs. 3 and 4, the frequency components far from the center frequency f_{IF} will be greatly attenuated. On the other hand, at the output of the IF filter, the frequency components outside of 6-dB bandwidth may still have high magnitudes so they may not be ignored. Because the measurement uncertainty of the spectrum analyzer used in this paper is 1.5 dB, it is unnecessary to consider the frequency components outside of two RBW in EMI prediction because at the boundary frequencies of 2 RBW, the IF filter has around -20 dB attenuation and the frequency components at the boundary frequencies of two RBW contribute no more than 1.5 dB to the output of the IF filter if they have the same magnitude as that at center frequency before feeding to the IF filter. Two RBW is thus defined as the effective bandwidth of the IF filters in this paper. The products of the Gaussian function in (1) and the extracted frequency components from FFT, which are sinusoidal functions, is the output of the IF filter.

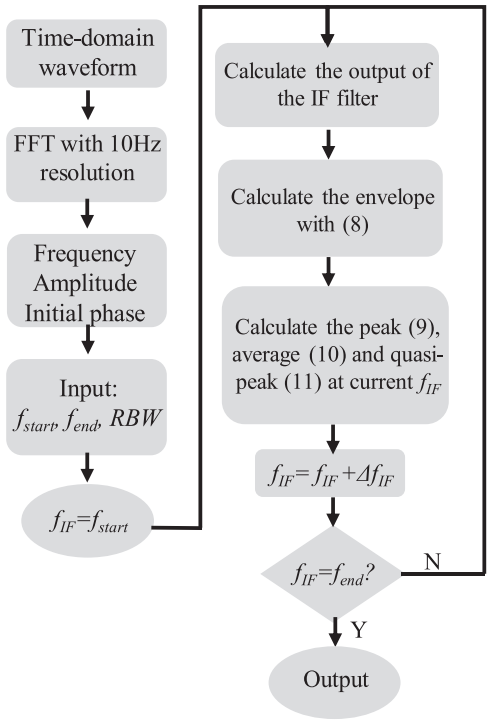

Fig. 8. Flowchart of EMI noise spectrum prediction algorithm.

The envelope can be calculated based on the frequency components from the IF filter within the effective bandwidth from (8). The peak value, quasi-peak value, and average values within one or multiple periods can be calculated from (9), (10), and (11). Usually, the data from one period is used for calculation to achieve the fastest speed. In the next step, the whole process will be repeated at frequency $f_{\text{IF}} = f_{\text{IF}} + \Delta f_{\text{IF}}$, where Δf_{IF} is the desired frequency step, until the EMI within all concerned frequency range is predicted.

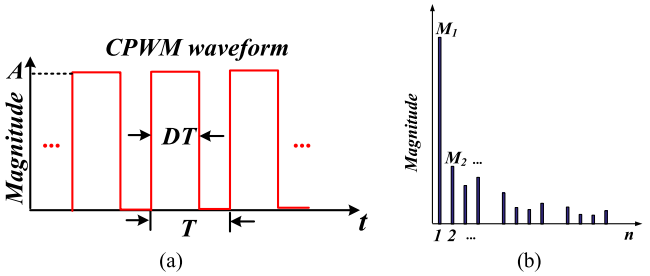

Fig. 9. (a) CPWM time-domain waveform ($D = 0.6$) and (b) its spectrum.

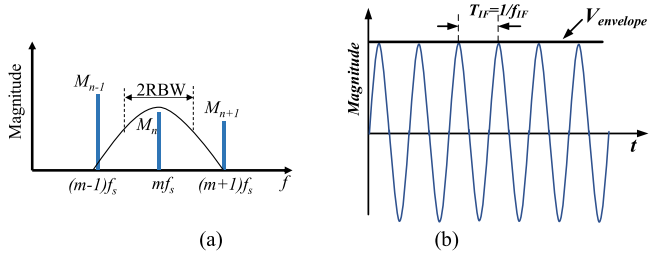

Fig. 10. (a) IF filter has a smaller effective bandwidth than harmonic frequency interval. (b) The envelope waveform.

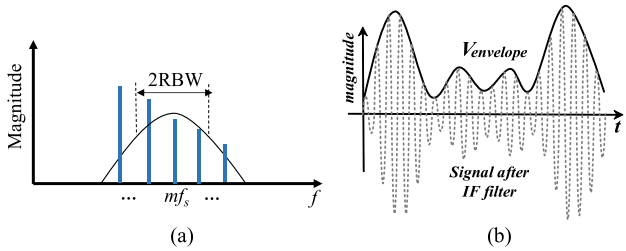

Fig. 11. (a) IF filter has a larger effective bandwidth than harmonic frequency interval. (b) IF filter output.

III. Sideband and RBW's Effects on EMI Measurement

Based on the analysis in Section II, the RBW and the input noise spectrum mostly determine the output waveform of the envelope detector, which in turn determines the outputs of the peak, quasi-peak, and average detectors. In EMI modeling for power electronics systems, the non-linear power semiconductor switches can be replaced with linear equivalent noise voltage or current sources [1], [5]. Since EMI is generated from these noise sources and the measured EMI on LISNs is determined by these noise sources and the noise propagation network from the noise sources to LISNs, it is necessary to investigate the relationship between the spectrum of EMI noise sources and some commonly used modulation schemes in power electronics systems based on effective bandwidth 2 RBW. In this section, it will be proved that FFT results are always smaller than, peak, quasi-peak, and average values when multiple frequency components are within the effective bandwidth. The differences between FFT results and average values will be theoretically analyzed for CPWM in dc/dc conversion and SPWM in ac/dc and dc/ac conversion. It has been proved in Section II-C that, $V_{\text{peak}} \geq V_{\text{quasi-peak}} \geq V_{\text{ave}}$ and the equality holds only when the output voltage V_i of the envelope detector is dc.

For simplification, the rising and falling time of the switching waveform is assumed to be zero. This simplification will not influence the harmonic frequency distribution.

A. Constant Pulsewidth Modulation

In Fig. 9(a), CPWM waveform has magnitude A, a fixed frequency $f_s = 1/T$ and duty cycle D.

The spectrum in Fig. 9(b) can be derived in (12) and (13) in terms of harmonic magnitude M_n and phase φ_n, where n is the order of harmonics

$$M_n = 2\text{AD}\left|\frac{\sin(n\pi D)}{n\pi D}\right| \tag{12}$$

$$\varphi_n = \pm n\pi D. \tag{13}$$

For conductive EMI, the switching frequency is usually much higher than the RBW in the EMI standard (200 Hz RBW from 9 to 150 kHz, 9 kHz RBW from 150 kHz to 30 MHz). If $k = 2\,\text{RBW}/f_s \leq 1$, only single frequency component is within the two RBW effective bandwidth of the IF filter in Fig. 10(a). Because of this, the output time-domain waveform of the IF filter (before the envelope detector) has only one frequency component as shown in Fig. 10(b). And because this single frequency component has constant magnitude, based on (8), the envelope V_{envelope} of the waveform is dc.

As analyzed previously, based on (9), (10), and (11) in Section II, the peak, quasi-peak, and average values of a dc envelope signal are equal, which means that these three measurement results are equal when two RBW is smaller than the switching frequency of the CPWM waveform. In this case, the measurement results are also equal to FFT results because FFT generates the spectrum of the magnitudes of all individual frequency components. In a word, $V_{\text{peak}} = V_{\text{quasi-peak}} = V_{\text{ave}} = V_{\text{FFT}}$ when $k \leq 1$.

For radiated EMI, the RBW could be several times larger than switching frequency (120 kHz RBW from 30 MHz to 1 GHz in CISPR16), so multiple frequency components may be within the two RBW effective bandwidth as in Fig. 11(a). Based on (8), because the output of the IF filter contains multiple frequency components, its envelope has both dc and ac as shown in Fig. 11(b).

Since the envelope is periodic, if there are q number of frequency components in 2 RBW, the average value (10) of the envelope in (8) can be rewritten as (14), which contains only dc component

$$V_{\text{ave}} = \sqrt{\sum_{i=1}^{q} A_i^2}. \tag{14}$$

Equation (14) shows that the average value is determined by the magnitude of the frequency components at the output of the IF filter within 2 RBW. It should be noted that the frequency components outside two RBW could be much larger than the center

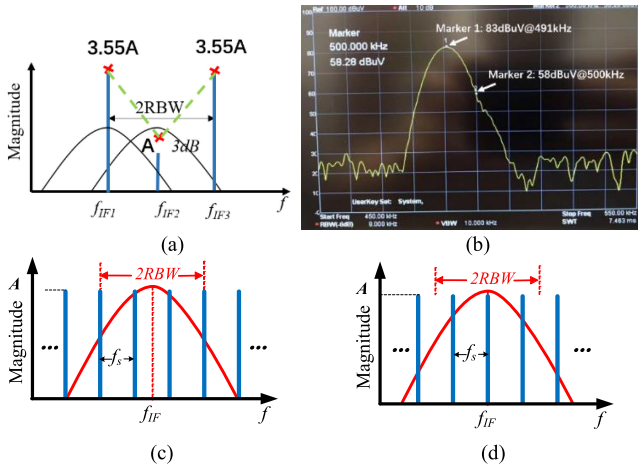

Fig. 12. Effects of the locations of frequency components on the measurement result at center frequency. (a) Two large boundary signals' effects on the measurement result at center frequency. (b) One large boundary signal's skirt covers the small center frequency signal. (c) No frequency component at f_{IF}. (d) One frequency component at f_{IF}.

frequency component, however, their influence to the measurement result is limited. For example, in Fig. 12(a), the signal at center frequency f_{IF2} of the IF filter has a magnitude of A. If the signals at two RBW boundary has a magnitude of 3.55 A, they will increase the output of the IF filter at f_{IF2} by 3 dB. Because the spectrum analyzer sweeps the frequency, the signals at f_{IF1} and f_{IF3} will also be located at the center frequency of the IF filter when they are swept. As a result, there will be two noise peaks on the two sides of f_{IF2}. They are 8 dB higher than the signal at f_{IF2}. This means that the measured spectrum will have noise peaks at f_{IF1} and f_{IF3} and a noise valley at f_{IF2}. So, the signal at f_{IF2} is not important in noise diagnosis and EMI filter design. This can also be proved by the measurement in Fig. 12(b). When the frequency component (Marker 1) at the boundary of the two RBW is 25 dB larger than the frequency component (Marker 2) at center frequency, the measured EMI at center frequency is smaller than the skirt of the measured EMI at the boundary frequency.

The average value in (14) can be further calculated by (15), where M_i is the magnitude of the ith harmonic in effective bandwidth. G_i from (1) is the gain of the IF filter to ith harmonic. Equation (15) indicates that average value at f_{IF} will be always larger than FFT value if multiple frequency components are within the effective 2 RBW

$$V_{\mathrm{ave-fIF}} = \sqrt{(G_1M_1)^2 + \cdots + {M_{\mathrm{fIF}}}^2 + \cdots + (G_qM_q)^2} > V_{\mathrm{FFT}} = M_{\mathrm{fIF}}. \tag{15}$$

Parameter k can be used to characterize the difference between the average and FFT value. A larger k means more frequency components are in the 2 RBW, and it increases the average value in (15). If $k \leq 1$, there is only one frequency component in 2 RBW. If $1 < k \leq 2$, there may have one or two frequency components in 2 RBW. When k is other values, it can be analyzed similarly. It can be proved in (16), (17), (18), Figs. 12 (c), (d),

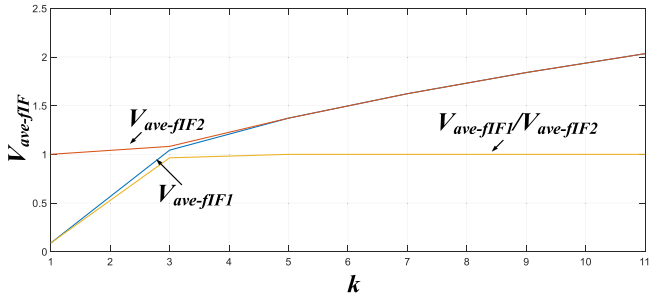

Fig. 13. $V_{\mathrm{ave\text{-}fIF}}$ reaches the highest when there is a frequency component at f_{IF}.

and 13 that if the frequency components fed to the IF filter have the identical magnitude A, the worst (highest) average $V_{\mathrm{ave\text{-}fIF}}$ at f_{IF} happens when there is a frequency component at f_{IF}. This means if $k \leq 2$, the worst EMI is equal to the $V_{\mathrm{ave\text{-}fIF}}$ at f_{IF} when $k \leq 1$. Two cases are illustrated when $k = 3$ in Fig. 12 (c) and (d). There is no frequency component at f_{IF} in case 1 in Fig. 12 (c) and there is a frequency component at f_{IF} in case 2 in Fig. 12 (d). $V_{\mathrm{ave\text{-}fIF2}}$ is higher in case 2 than $V_{\mathrm{ave\text{-}fIF1}}$ in case 1 as proved in (16). In (16), G(f) is the IF filter gain defined in (1). f is the frequency difference between f_{IF} and the frequency components. Fig. 13 shows $V_{\mathrm{ave\text{-}fIF1}}$, $V_{\mathrm{ave\text{-}fIF2}}$, and their ratio. $V_{\mathrm{ave\text{-}fIF}}$ reaches the highest when a frequency component is at f_{IF} as shown in (17), (18) and Fig. 13. If $k > 3$, the differences between $V_{\mathrm{ave\text{-}fIF1}}$ and $V_{\mathrm{ave\text{-}fIF2}}$ is small so it can be ignored

$$\begin{aligned} V_{\mathrm{ave-fIF1}} &= A\sqrt{2G^2\left(\frac{1}{3}RBW\right) + 2G^2(RBW)} \\ &= 1.043A < V_{ave-fIF2} = A\sqrt{1 + 2G^2\left(\frac{2}{3}RBW\right)} \\ &= 1.0817A \end{aligned} \tag{16}$$

$$V_{\mathrm{ave-fIF1}} = A\sqrt{2\sum_{i=1}^{\frac{k+1}{2}} e^{-\left(\frac{c^2(2i-1)^2}{k^2}\right)}} \tag{17}$$

$$V_{\mathrm{ave-fIF2}} = A\sqrt{1 + 2\sum_{i=1}^{\frac{k+1}{2}} e^{-\left(\frac{c^2 4i^2}{k^2}\right)}}. \tag{18}$$

At the worst scenario, when there is a frequency component at f_{IF}, based on (12) and (15), the ratio of $V_{\mathrm{ave\text{-}fIF}}/V_{\mathrm{FFT}}$ can be calculated in Fig. 14 (a) in terms of k and duty cycle D. Fig. 14(b) shows the FFT spectrum and the measured average spectrum using a spectrum analyzer for a CPWM waveform at $f_s = 1$ kHz, $D = 0.3$ from a signal generator. From 9 to 150 kHz, $k = 2 \times 200$ Hz/1 kHz $= 0.4$. There is no difference between the average and FFT result as expected previously. From 150 kHz to 30 MHz, $k = 2 \times 9$ kHz/1 kHz $= 18$, there is 4 dB difference between the average and FFT result as predicted in Fig. 14 (a). Based on Fig. 14 (a), if $k > 6$, the FFT result is more than 3 dB smaller than the average value, and based on the analysis previously, it could be even much smaller than quasi-peak and peak values, so the FFT result is considered inaccurate for EMI prediction under this condition.

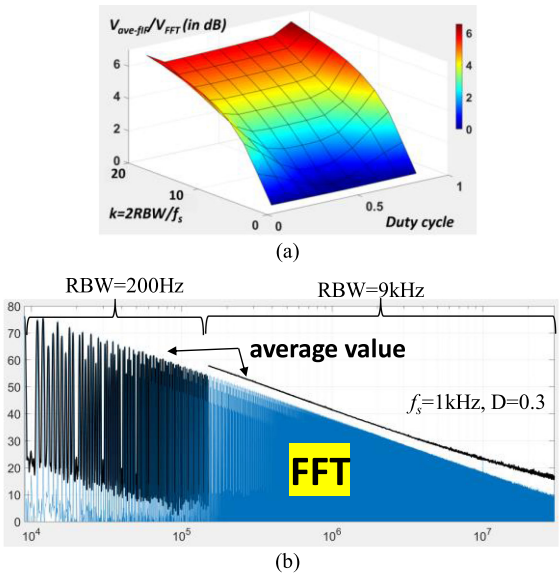

Fig. 14. (a) Calculated $V_{\text{ave-fIF}}/V_{\text{FFT}}$ as a function a D and k. (b) Measured $V_{\text{ave-fIF}}$ and V_{FFT}.

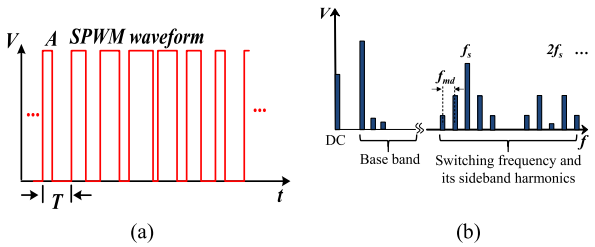

Fig. 15. (a) SPWM time-domain waveform. (b) Spectrum of the SPWM waveform.

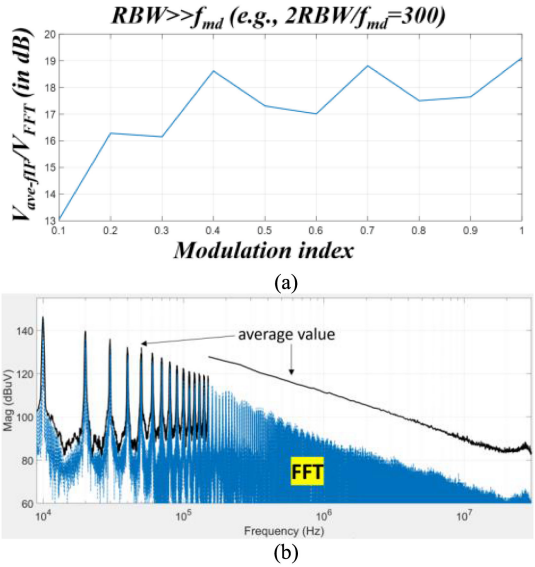

Fig. 16. (a) Calculated $V_{\text{ave-fIF}}/V_{\text{FFT}}$ as a function of modulation index. (b) Measured $V_{\text{ave-fIF}}$ and V_{FFT} of the SPWM waveform.

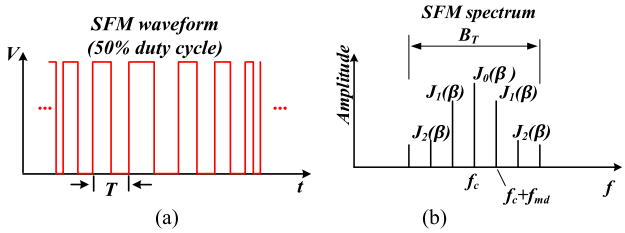

Fig. 17. (a) SFM time-domain waveform. (b) Spectrum.

In summary, when $k > 2$, $V_{\text{peak}} > V_{\text{quasi-peak}} > V_{\text{ave}} > V_{\text{FFT}}$. When $k \leq 2$, $V_{\text{peak}} = V_{\text{quasi-peak}} = V_{\text{ave}} = V_{\text{FFT}}$.

B. Sinusoidal Pulsewidth Modulation

SPWM waveform can have significant sideband effects because the duty cycle is modulated with a sine function, which has modulation frequency f_{md}. The waveform of SPWM at switching frequency $f_s = 1/T$ is shown in Fig. 15 (a) and Fig. 15 (b) shows the spectrum of the SPWM waveform.

The spectrum can be analyzed using double edge Fourier analysis [14]. Similar to CPWM waveforms, if $k = 2\,\text{RBW}/f_{\text{md}} > 2$, the FFT results are smaller than the average values and the envelope of the output of the IF filter is composed of a dc component and ac components similar to that in Fig. 11(b) because there are multiple frequency components within the effective bandwidth two RBW of the IF filter.

The differences between FFT and the average value can be derived based on (15) and the SPWM harmonic equations in [14]. Fig. 16(a) shows the calculated differences in terms of modulation index M when $k = 300$. Fig. 16 (b) shows experimental results of a SPWM waveform at $M = 0.7$. From 9 to 150 kHz, $k = 2 \times 200$ Hz/60 Hz $= 6.67$, there is 4 dB difference between $V_{\text{ave-fIF}}$ and V_{FFT}. From 150 kHz to 30 MHz, $k = 2 \times 9$ kHz/60 Hz $= 300$, there is 16 dB difference between $V_{\text{ave-fIF}}$ and V_{FFT} compared with the predicted 19 dB difference in Fig. 16 (a) at $M = 0.7$.

It has been proved above that conventional FFT results are not the same as the measured EMI with a spectrum analyzer following EMI standards. It has been verified that the FFT results are no more than the average EMI values in power electronics applications. The differences between the FFT results and average values can be estimated with the theory developed in this section.

C. Switching Frequency Modulation

SFM techniques [17], [18] are applied in power electronics systems to spread the spectrum and reduce EMI noise. The duty cycle of the SFM waveform remains constant in each switching period in Fig. 17(a), but the switching frequency f_{s} is a function of time. Different SFM strategies, such as sinusoidal modulation, linear modulation, exponential modulation, random modulation, and dc offset, are discussed in literatures [18]–[20], [23] to reduce EMI. The sinusoidal modulation will be analyzed here. Other modulations can be analyzed similarly.

For sinusoidal SFM, the switching frequency f_{s} is given by

$$f_s = f_c + \Delta f \sin(2\pi f_{\text{md}} t) \tag{19}$$

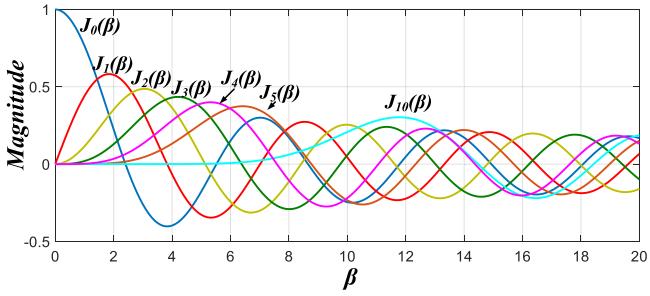

Fig. 18. First kind Bessel functions.

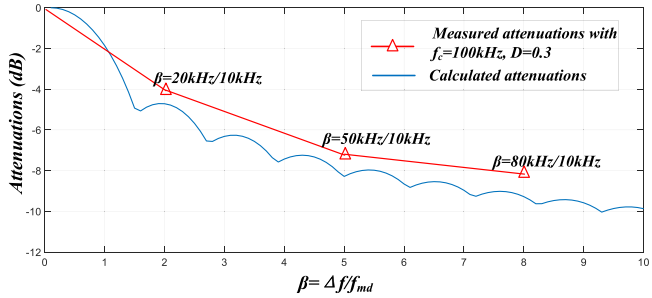

Fig. 19. Comparison of calculated attenuation and measured attenuation with different β.

where f_c is the center switching frequency, Δf is the frequency deviation, and $f_{\rm md}$ is the modulation frequency. The spectrum for the harmonics around f_c is shown in Fig. 17 (b). $\beta = \Delta f / f_{\rm md}$ is modulation index. J is Bessel function. The frequency interval of adjacent harmonics is $f_{\rm md}$. The Carson's bandwidth B_T, which is given by (20) includes $\geq$98% energy based on Rayleigh's energy theorem and Carson's rule. The Carson's bandwidth B_T of the sideband of the *n*th-order switching harmonics is nB_T.

$$B_T = 2\left(\Delta f + f_{\rm md}\right). \tag{20}$$

To reduce EMI, the energy within two RBW should be as small as possible, so B_T should meet condition (21)

$$B_T \gg 2\mathrm{RBW}. \tag{21}$$

Furthermore, as analyzed previously, for SFM, because the frequency distance between two adjacent frequency components is $f_{\rm md}$, if $f_{\rm md}$ is equal or larger than two RBW ($k = 2\ \mathrm{RBW}/f_{\rm md} \leq 1$), there is only one frequency component within 2 RBW, the energy within two RBW is minimized. When $1 < k \leq 2$, as analyzed previously, if there is a frequency component at $f_{\rm IF}$, EMI will be equal to that when $k \leq 1$. If there is no frequency component at $f_{\rm IF}$, there may have two frequency components within 2 RBW, but EMI will be lower than that when there is a frequency component at $f_{\rm IF}$. Because of this, $f_{\rm md}$ should be chosen based on

$$k = 2\mathrm{RBW}/f_{\rm md} \leq 2. \tag{22}$$

Finally, if frequency deviation Δf increases, β will increase. This can lead to a magnitude decreased Bessel function in Fig. 18. As an example, it is shown in Fig. 18 that if $\beta >$ 10 the noise spectrum in Fig. 17 (b) will have an approximate even distribution within J_0, ..., J_{10}. This helps reduce EMI.

The measured and calculated EMI attenuations for peak values by using SFM at $f_c = 100$ kHz, $k = 2$, and $f_{\rm md} = 10$ kHz from conventional CPWM with $f_s = 100$ kHz and $D = 0.3$ are compared in Fig. 19 as a function of β when Δf changes. In Fig. 19, the calculated matches the measured. Since $k \leq 2$, peak value = quasi-peak value = average value. It is shown that increasing β can reduce EMI. It is also shown that the attenuation tends to be saturated as β increases to above ten, which agrees with Fig. 18.

Based the analysis above, to minimize EMI with SFM, the following conditions should be met:

1) $B_T >> 2$ RBW to reduce the total energy within two RBW.
2) $K \leq 2$ to reduce the number of frequency components within two RBW.
3) $\beta \geq 10$ to reduce the magnitudes of the frequency components within two RBW.

If conditions 2) and 3) were met, the condition 1) will be automatically met. If only part of these conditions were met, the EMI may still be reduced but not minimized.

In summary, the FFT result will be equal to peak, quasi-peak, and average values if $k \leq 2$ and it will be smaller than peak, quasi-peak, and average values if $k > 2$, where $k = 2\ \mathrm{RBW}/f_s$ in CPWM case, and $k = 2\ \mathrm{RBW}/f_{\rm md}$ in SPWM and SFM cases. Because a spectrum analyzer can only measure EMI at a limited number of frequencies, the measurement results may miss some noise spike information, so a small frequency step, for example, RBW/4, is recommended to improve measurement accuracy.

IV. Experimental Verifications

In this section, the proposed EMI prediction and analysis techniques in Sections II and III will be evaluated in experiments. The proposed technique takes a very short time to accurately predict the peak, quasi-peak, and average values.

A. Experimental Verifications for CPWM Waveforms

Two experiments were conducted. In the first experiment, the developed theory is validated with a CPWM waveform generated by a signal generator. In the 2nd experiment, the developed theory is validated with a dc/dc boost converter. Fig. 20(a) shows the 1st measurement setup. A signal generator generated two CPWM waveforms with different frequencies, magnitudes, and duty cycles as in Fig. 20 (b) and the waveforms were fed to a spectrum analyzer.

Fig. 21 shows the comparison of the predicted and measured EMI for CPWM waveform with 10 kHz frequency, 50% duty cycle and 100 mV magnitude. The spectrum was measured using a RIGOL DSA800 spectrum analyzer based on CISPR16 RBW requirements. The time-domain waveform used for EMI prediction is measured with the oscilloscope Rigol MSO4054

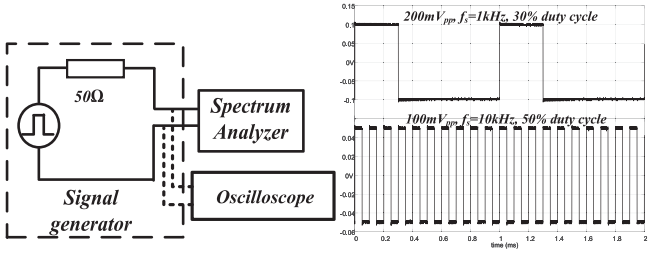

Fig. 20. (a) CPWM spectrum measurement setup. (b) Time-domain waveforms.

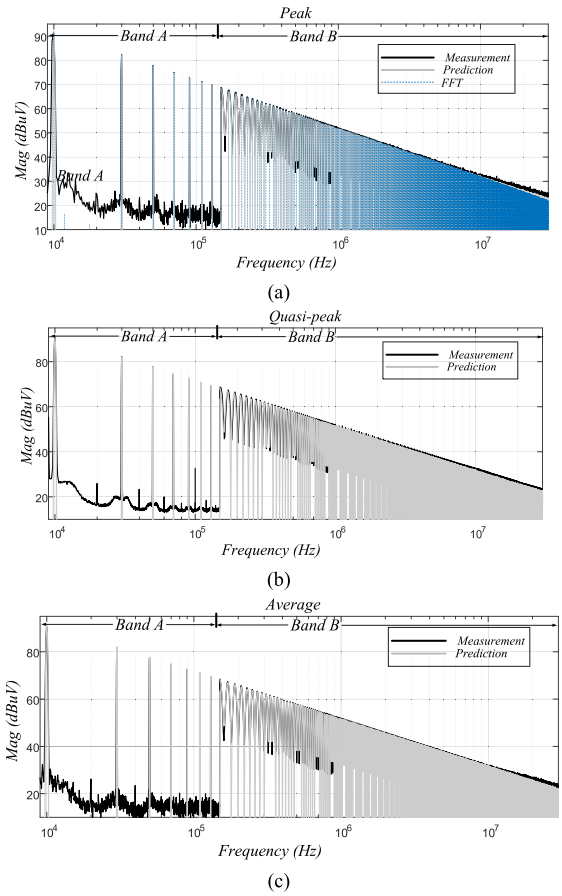

Fig. 21. EMI comparison of the predicted, measured, and FFT results for 10 kHz CPWM waveform. (a) Peak value. (b) Quasi-peak value. (c) Average value.

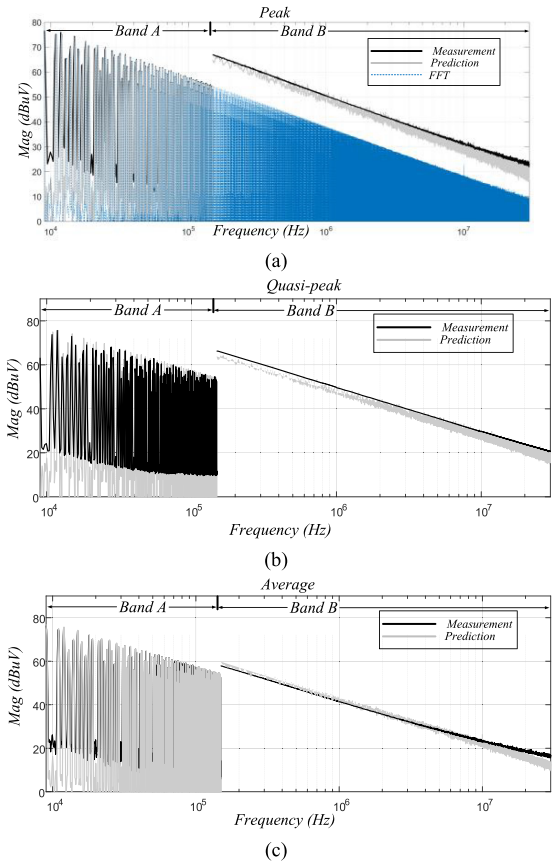

Fig. 22. EMI comparison of the predicted, measured, and FFT results for 1 kHz CPWM waveform. (a) Peak value. (b) Quasi-peak value. (c) Average value.

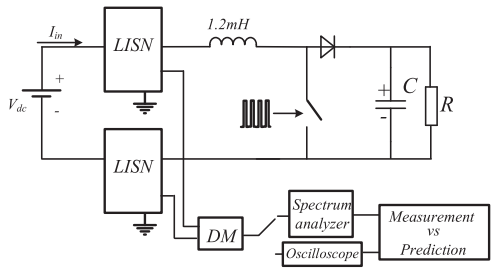

Fig. 23. Measurement setup for a dc–dc boost converter with CPWM.

via a coaxial cable with 50 Ω characteristic impedance connected between LISNs and the oscilloscope. The oscilloscope's input channel has 50 Ω input impedance, so there is no reflection or distortion on the measured signals. The background noise of the Rigol MSO4054 oscilloscope is less than 15 dBμV at 50 mV/div scale. At this scale, it can measure EMI at up to 106 dBμV, so the background noise will not influence the predicted EMI and the evaluation of the proposed technique. The predicted matches the measured. Because the RBW is 200 Hz in band A (9–150 kHz) and 9 kHz in band B (150 kHz–30 MHz), respectively, $k = 2\,\mathrm{RBW}/f_s \leq 2$. As analyzed in Section III, peak, quasi-peak, and average values are all equal to the FFT results. Since the spectrum of a fixed frequency and fixed duty cycle waveform can be expressed in (12), the peak value of the spectrum decreases at –20 dB/decade in both band A and B.

When switching frequency is 1 kHz with 30% duty cycle and 200 mV magnitude in Fig. 22, in band A, $k = 2\,\mathrm{RBW}/f_s \leq 2$, so the peak, quasi-peak, and average values are equal, but in band B, $k = 2\,\mathrm{RBW}/f_s = 18 > 2$, so peak > quasi-peak > average > FFT result as analyzed in Section III. As a result, in experiments, the measured EMI is discontinuous at the boundary 150 kHz between band A and band B (a 12 dB difference is observed). The predicted matches the measured.

The proposed technique is further verified in a dc/dc boost converter in the 2nd experiment. The measurement setup is shown in Fig. 23. The boost converter has 12 V input voltage, 15 V output voltage, and 23 W output power. The duty cycle is 0.8 and switching frequency $f_s = 20$ kHz. The

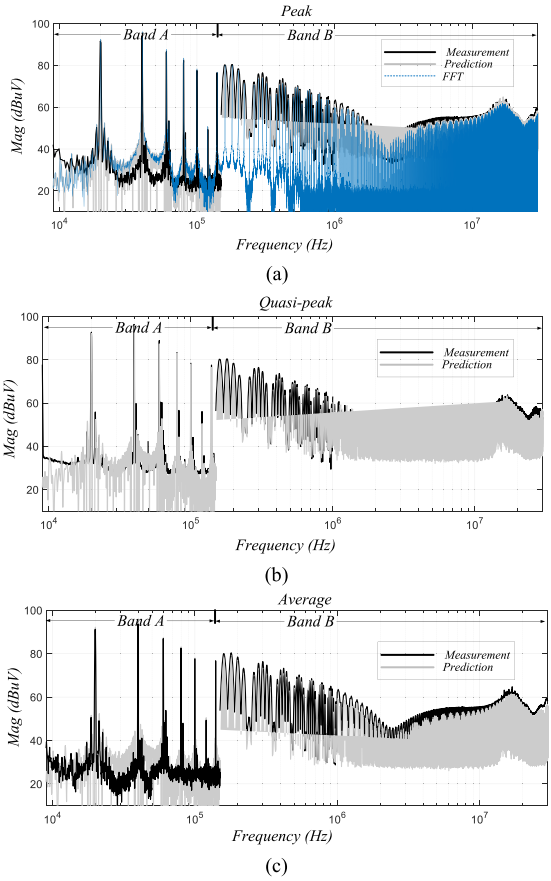

Fig. 24. DM noise of a boost converter. (a) Peak value. (b) Quasi-peak value. (c) Average value.

differential mode (DM) noise was separated with a noise separator [24]–[26] from the total EMI noise on LISNs and fed to the spectrum analyzer for EMI measurement. It should be noted that DM/common mode (CM) separator is not necessary in standard EMI measurement. In this paper, to demonstrate the effectiveness of the proposed technique in EMI diagnosis, a noise separator is used for measuring the DM noise of a dc/dc converter and the noise of an ac/dc converter. The time domain waveform used for EMI prediction is measured with the oscilloscope Rigol MSO4054 via a coaxial cable with 50 Ω characteristic impedance connected between LISNs and the oscilloscope. As stated previously, because the oscilloscope's input impedance is 50 Ω, there is no reflection or distortion on the measured signals. Fig. 24 (a), (b), and (c) compare the FFT, the predicted and the measured EMI. Since $k = 2\,\mathrm{RBW}/f_s < 2$ in both band A and B, peak value = quasi-peak value = average value = FFT values. The difference between the predicted and measured is less than 3 dB.

B. Experimental Verification for SPWM Waveforms

The developed theory for SPWM waveform is also verified with an ac/dc rectifier in Fig. 25. The ac/dc converter has 120 V/60 Hz input voltage, 300 V output dc voltage, 900 W output power and $f_s = 10$ kHz. The boost inductor L is 10 mH. C_{rec} is the parasitic capacitance between the collectors

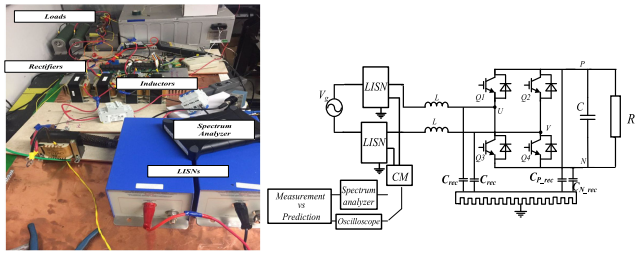

Fig. 25. (a) Measurement setup for SPWM waveform in an ac/dc rectifier system. (b) The circuit topology.

TABLE III
SCAN TIME OF CISPR 16 EMI MEASUREMENT USING RIGOL DSA800

Band	*Frequency*	*Scan time for peak detection*	*Scan time for quasi-peak detection*	*Scan time for average detection*
A	*9kHz-150kHz*	*14.1s*	*2820s=47mins*	*8.1s*
B	*150kHz-30MHz*	*2.985s*	*5970s=1h39mins*	*33.16s*

of insulated-gate bipolar transistors (IGBTs) and the grounded heatsink. $C_{\mathrm{P\_rec}}$ and $C_{\mathrm{N\_rec}}$ are the parasitic capacitance between the dc bus and the grounded heatsink. The H-bridge operated with SPWM at 60 Hz and equivalent $f_{\mathrm{md}} = 120$ Hz for CM noise due to the symmetrical operation of the two legs. Two LISNs are located between the power grid and the rectifier for noise measurement. The CM noise was separated from the total noise using a noise separator [24]–[26] and fed to the spectrum analyzer. The time-domain waveform from the output of the noise separator was saved to an oscilloscope for EMI prediction.

Based on the saved time-domain waveform, the frequency, magnitude, and initial phase information can be derived using FFT. The EMI is predicted based on the proposed technique in Sections II and III. It is compared with the FFT and the measured results in Fig. 26. The predicted and measured match well.

In Fig. 26, for band A, because $k = 3.3 > 2$, FFT result is smaller than peak, quasi-peak, and average values. In band B, because $k = 150 >> 2$, FFT result is much smaller than peak, quasi-peak, and average values.

In Table III, compared with actual time used in a standard EMI measurement, the proposed technique can accurately predict the peak, quasi-peak, and average values of the EMI noise simultaneously in less than 2 min in band A and less than 5 min in band B. It saves a lot of time. Also, the proposed technique can be implemented with an oscilloscope and a personal computer, so it saves the expense of an expensive spectrum analyzer and give engineers more freedom in EMI measurement and debugging.

C. Experimental Verification for SFM

The measured and predicted EMI are compared in Fig. 27 for SFM waveform with the same setup as in Fig. 20 (a). The SFM voltage waveform has a modulation frequency $f_{\mathrm{md}} =$ 5 kHz, frequency deviation $\Delta f = 50$ kHz, center switching frequency $f_c = 100$ kHz, a modulation index $\beta = \Delta f / f_{\mathrm{md}} = 50\,\mathrm{kHz}/5\,\mathrm{kHz} = 10$, 3.3 V magnitude, and 0.7 duty cycle.

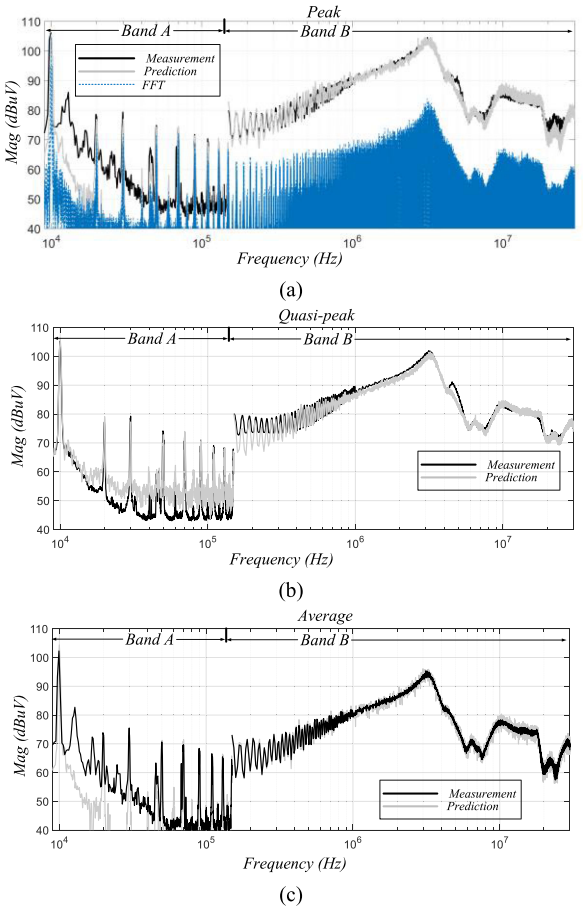

Fig. 26. CM noise of an ac/dc rectifier with SPWM. (a) Peak values. (b) Quasi-peak values. (c) Average values.

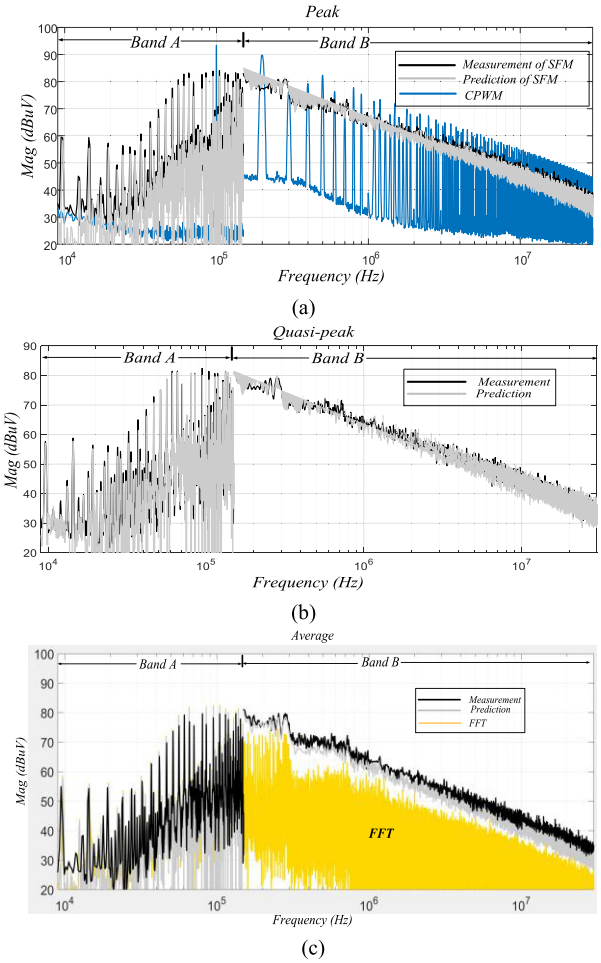

Fig. 27. SFM EMI measurement results. (a) Peak values. (b) Quasi-peak values. (c) Average values.

In Fig. 27, for band A, $k = 400$ Hz/5 kHz $= 0.08$, so peak value = quasi-peak value = average value = FFT results as predicted. There is more than 10 dB attenuation due to frequency modulation, which spreads the EMI spectrum, compared with CPWM waveform, which has an EMI spike at switching frequency 100 kHz. In band B, $k = 18$ kHz/5 kHz $= 3.6$. Because multiple frequency components are within 2 RBW, the EMI attenuation due to using SFM is not as good as that in band A as shown in Fig. 27 (a). At the same time, the FFT result is smaller than the average values in Fig. 27 (c) as expected. In the three figures, the difference between the predicted and measured results is less than 5 dB, which verifies the proposed EMI prediction technique.

Compared with the measured EMI noise, the proposed technique can accurately predict the EMI although there is up to 3 dB difference at high frequencies. Several factors may lead to the difference. First, the Rigol DSA800 has a measurement uncertainty of 1.5 dB. Second, the number of the sampling points on the envelope waveform influences the calculated results. In this paper, 1000 sampling points are selected to achieve a balance between good calculation accuracy and calculation speed. Third, the analog-digital conversion (ADC) resolution of the oscilloscope will influence the accuracy of the saved time-domain waveform. The small signals may not be properly sampled due to the limited digital resolution of ADC. Moreover, the FFT applied to the input time-domain waveform may also bring phase error at high-order harmonics. The phase error will influence the output of the IF filter and the detectors. However, since the difference between the calculation and measurement is small, it is not an issue.

V. Conclusion

In this paper, the EMI prediction technique is developed based on the operating principle of EMC spectrum analyzers. Compared with existing literature, the IF filter and envelope detector are accurately modeled. The EMI prediction procedure is proposed based on time-domain waveforms. The effects of sideband and effective RBW on the measured EMI are analyzed. The EMI of CPWM, SPWM, and SFM are analyzed and compared with FFT results. It is proved in this paper that the conventional FFT results can be different from the measured peak, quasi-peak, and average values using spectrum analyzer. The difference could be significant if the parameter $k = 2\,\mathrm{RBW}/f_s$ or $2\,\mathrm{RBW}/f_{\mathrm{md}}$ is big. Generally, the FFT results are no more than the average EMI values. Experiments were conducted to verify the developed EMI prediction and analysis techniques.

REFERENCES

[1] H. Zhang, L. Yang, S. Wang, and J. Puukko, "Common-mode EMI noise modeling and reduction with balance technique for three-level neutral point clamped topology," *IEEE Trans. Ind. Electron.*, vol. 64, no. 9, pp. 7563–7573, Sep. 2017.

[2] L. Yang, S. Wang, and J. Feng, "Electromagnetic interference modeling and suppression techniques in variable-frequency drive systems," *Front. Mech. Eng.*, vol. 13, no. 3, pp. 329–353, 2018.

[3] "CISPR16-1-1" in Specification for Radio Disturbance and Immunity Measuring Apparatus and Methods Part 1-1: Radio Disturbance and Immunity Measuring Apparatus-Measuring Apparatus, Switzerland: Int. Electrotech. Commiss., 2003.

[4] Y. Maillet, R. Lai, S. Wang, F. Wang, R. Burgos and D. Boroyevich, "High-density EMI filter design for DC-fed motor drives," *IEEE Trans. Power Electron.*, vol. 25, no. 5, pp. 1163–1172, May 2010.

[5] L. Yang, H. Zhao, S. Wang, Y. Zhi, B. Zhu, and J. Min, "Develop common-mode EMI noise models for AC-DC-AC traction systems," in *Proc. 43rd Annu. Conf. IEEE Ind. Electron. Soc.*, Beijing, China, 2017, pp. 7012–7017.

[6] Q. Liu, F. Wang, and D. Boroyevich, "Conducted-EMI prediction for AC converter systems using an equivalent modular–terminal–behavioral (MTB) source model," *IEEE Trans. Ind. Appl.*, vol. 43, no. 5, pp. 1360–1370, Sep./Oct. 2007.

[7] Rohde & Schwarz, Spectrum Analyzer Fundamentals – Theory and Operation of Modern Spectrum Analyzers.

[8] F. Giezendanner, J. Biela, J. W. Kolar, and S. Zudrell-Koch, "EMI noise prediction for electronic ballasts," *IEEE Trans. Power Electron.*, vol. 25, no. 8, pp. 2133–2141, Aug. 2010.

[9] Keysight, Spectrum Analyzer Basics, Appl. Note 150, pp. 18, 2014.

[10] H. Li and K. Y. See, "Conversion factors between common detectors in EMI measurement for impulse and Gaussian noises," *IEEE Trans. Electromagn. Compat.*, vol. 55, no. 4, pp. 657–663, Aug. 2013.

[11] T. Karaca, B. Deutschmann and G. Winkler, "EMI-receiver simulation model with quasi-peak detector," in *IEEE Int. Symp. Electromagn. Compat.*, Dresden, 2015, pp. 891–896.

[12] Z. Wang, S. Wang, P. Kong, and F. C. Lee, "DM EMI noise prediction for constant on-time, critical mode power factor correction converters," *IEEE Trans. Power Electron.*, vol. 27, no. 7, pp. 3150–3157, Jul. 2012.

[13] Q. Ji, X. Ruan, and Z. Ye, "The worst conducted EMI spectrum of critical conduction mode boost PFC converter," *IEEE Trans. Power Electron.*, vol. 30, no. 3, pp. 1230–1241, Mar. 2015.

[14] D. G. Holmes and T. A. Lipo, *Pulse Width Modulation for Power Converters: Principles and Practice*, vol. 18. New York, NY, USA: Wiley, 2003.

[15] T. Nussbaumer, K. Raggl, and J. W. Kolar, "Design guidelines for interleaved single-phase boost PFC circuits," *IEEE Trans. Ind. Electron.*, vol. 56, no. 7, pp. 2559–2573, Jul. 2009.

[16] T. Nussbaumer, M. L. Heldwein, and J. W. Kolar, "Differential mode input filter design for a three-phase buck-type PWM rectifier based on modeling of the EMC test receiver," *IEEE Trans. Ind. Electron.*, vol. 53, no. 5, pp. 1649–1661, Oct. 2006.

[17] F. Pareschi, R. Rovatti, and G. Setti, "EMI reduction via spread spectrum in DC/DC converters: State of the art, optimization, and tradeoffs," *IEEE Access*, vol. 3, pp. 2857–2874, 2015.

[18] F. Lin and D. Y. Chen, "Reduction of power supply EMI emission by switching frequency modulation," *IEEE Trans. Power Electron.*, vol. 9, no. 1, pp. 132–137, Jan. 1994.

[19] K. B. Hardin, J. T. Fessler, and D. R. Bush, "Spread spectrum clock generation for the reduction of radiated emissions," in *Proc. IEEE Symp. Electromagn. Compat.*, Chicago, IL, 1994, pp. 227–231.

[20] F. Mihali and D. Kos, "Reduced conductive EMI in switched-mode DC–DC power converters without EMI filters: PWM versus randomized PWM," *IEEE Trans. Power Electron.*, vol. 21, no. 6, pp. 1783–1794, Nov. 2006.

[21] L. W. Couch, II, *Digital and Analog Communication Systems*. Upper Saddle River, NJ, USA: Prentice-Hall, 2000.

[22] RIGOL Technical Staff, *DSA800 Series Spectrum Analyzer*. Beijing, China: RIGOL Technologies, Inc., 2006.

[23] H. Zhao *et al.*, "A SPWM technique with DC offset based on total energy reduction for both the harmonic and EMI noise suppression," in *Proc. 43rd Annu. Conf. IEEE Ind. Electron. Soc.*, Beijing, 2017, pp. 6989–6994.

[24] S. Wang, F. C. Lee, and W. G. Odendaal, "Characterization, evaluation, and design of noise separator for conducted EMI noise diagnosis," *IEEE Trans. Power Electron.*, vol. 20, no. 4, pp. 974–982, Jul. 2005.

[25] S. Wang, F. Luo, and F. C. Lee, "Characterization and design of three-phase EMI noise separators for three-phase power electronics systems," *IEEE Trans. Power Electron.*, vol. 26, no. 9, pp. 2426–2438, Sep. 2011.

[26] S. Wang, "Modeling and design of EMI noise separators for multiphase power electronics systems," *IEEE Trans. Power Electron.*, vol. 26, no. 11, pp. 3163–3173, Nov. 2011.

[27] Tektronix, Fundamentals of Real-Time Spectrum Analysis, 2009.

Le Yang (S'16) received the B.S. degree from Xi'an Jiaotong University, Xi'an, China, in 2012, and the M.S. degree from the Huazhong University of Science and Technology, Wuhan, China, in 2015. He is currently working toward the Ph.D. degree in power electronics at the University of Florida, Gainesville, FL, USA.

His current research interests include electromagnetic interference modeling and suppression techniques in grid-tied power converters systems and motor drive systems, and magnetic components integration techniques.

Shuo Wang (S'03–M'06–SM'07–F'19) received the Ph.D. degree in electrical engineering from Virginia Tech, Blacksburg, VA, USA, in 2005.

Since 2015, he has been an Associate Professor with the Department of Electrical and Computer Engineering, University of Florida, Gainesville, FL, USA. From 2010 to 2014, he was with University of Texas at San Antonio, San Antonio, TX, USA, first as an Assistant Professor and later as an Associate Professor. From 2009 to 2010, he was a Senior Design Engineer with GE Aviation Systems, Vandalia, OH, USA. From 2005 to 2009, he was a Research Assistant Professor at Virginia Tech, Blacksburg, VA, USA.

Dr. Shuo Wang has published more than 180 IEEE journal and conference papers. He holds more than 20 issued and pending US patents. He was a recipient of the Best Transaction Paper Award from the IEEE Power Electronics Society in 2006, two William M. Portnoy awards for the papers published in the IEEE Industry Applications Society in 2004 and 2012, respectively, and the prestigious National Science Foundation CAREER Award, in 2012. He is an Associate Editor for the IEEE TRANSACTIONS ON INDUSTRY APPLICATIONS and a Technical Program Co-Chair for IEEE 2014 International Electric Vehicle Conference.

Hui Zhao (S'14) received the Ph.D. degree from the University of Florida, Gainesville, FL, USA, in 2018.

He had a summer internship with the General Electric (GE) Global Research Center Shanghai, Shanghai, China, in 2013. He is currently a Postdoctoral Research Associate with the University of Cambridge, Cambridge, U.K. He has authored and coauthored several IEEE conference and transaction papers.

Yongjian Zhi was born in Shangshui County, Henan, China, on July 15, 1982. He received the B.Sc. degree in electrical engineering and automation from Henan Polytechnic University, Jiaozuo, China, in 2006, and the Ph.D. degree from Zhejiang University, Hangzhou, China, in 2013.

He is a Senior Design Engineer working with CRRC Zhuzhou Institute Co., Ltd., Zhuzhou, Hunan, China. His research interests include electromagnetic compatibility and suppression techniques of rail transport.